

## Failure characteristics of reinforced concrete circular slabs subsequently subjected to fire exposure and static load

### An experimental study

Arano Barenys, Assis; Colombo, Matteo; Martinelli, Paolo; Øverli, Jan Arve; Hendriks, Max A.N.; Kanstad, Terje; di Prisco, Marco

**DOI**

[10.1002/suco.202200054](https://doi.org/10.1002/suco.202200054)

**Publication date**

2022

**Document Version**

Final published version

**Published in**

Structural Concrete

### Citation (APA)

Arano Barenys, A., Colombo, M., Martinelli, P., Øverli, J. A., Hendriks, M. A. N., Kanstad, T., & di Prisco, M. (2022). Failure characteristics of reinforced concrete circular slabs subsequently subjected to fire exposure and static load: An experimental study. *Structural Concrete*, 24(1), 872-891. <https://doi.org/10.1002/suco.202200054>

### Important note

To cite this publication, please use the final published version (if applicable). Please check the document version above.

### Copyright

Other than for strictly personal use, it is not permitted to download, forward or distribute the text or part of it, without the consent of the author(s) and/or copyright holder(s), unless the work is under an open content license such as Creative Commons.

### Takedown policy

Please contact us and provide details if you believe this document breaches copyrights. We will remove access to the work immediately and investigate your claim.

***Green Open Access added to TU Delft Institutional Repository***






***'You share, we take care!' - Taverne project***

**<https://www.openaccess.nl/en/you-share-we-take-care>**

Otherwise as indicated in the copyright section: the publisher is the copyright holder of this work and the author uses the Dutch legislation to make this work public.

## ARTICLE

# Failure characteristics of reinforced concrete circular slabs subsequently subjected to fire exposure and static load: An experimental study

Assis Arano Barenys<sup>1</sup> | Matteo Colombo<sup>2</sup>  | Paolo Martinelli<sup>2</sup>  |  
 Jan Arve Øverli<sup>1</sup>  | Max A. N. Hendriks<sup>1,3</sup>  | Terje Kanstad<sup>1</sup> |  
 Marco di Prisco<sup>2</sup> 

<sup>1</sup>Department of Structural Engineering, Norwegian University of Science and Technology, Trondheim, Norway

<sup>2</sup>Department of Civil and Environmental Engineering, Politecnico di Milano, Milan, Italy

<sup>3</sup>Faculty of Civil Engineering and Geosciences, Technical University of Delft, Delft, Netherlands

## Correspondence

Paolo Martinelli, Department of Civil and Environmental Engineering, Politecnico di Milano, Piazza L. da Vinci 32, 20133, Milan, Italy.

Email: [paolo.martinelli@polimi.it](mailto:paolo.martinelli@polimi.it)

## Funding information

Statens vegvesen; Norwegian Public Roads Administration

## Abstract

This study investigated the effect of fire on the ultimate load-bearing capacity of reinforced concrete (RC) slabs. The structural response of RC circular specimens subjected to static load conditions after exposure to a hydrocarbon fire on one side of the specimen was examined. Two fire exposure times were considered (60 and 120 min) in addition to reference non-exposed specimens. The static response was evaluated in the damaged specimens in residual conditions after natural cooling from the elevated temperatures. The temperature distribution across the thickness of the slabs and their load–displacement response was measured. The decrease in the stiffness of the slabs due to the thermal exposure was studied by means of direct ultrasonic pulse velocity (UPV) measurements made before and after the fire tests. The decrease in global stiffness was partially accounted for by UPV measurements. The experimental results showed two peaks in the load–deflection response of the slabs. The first peak was related to an arching mechanism introduced by the specific set-up used. The second peak, corresponding to the ultimate load, occurred due to tensile membrane action at large deflections. While the former was strongly affected by the fire exposure, with the load being halved after the 120-min exposure, the latter was not greatly affected by either the presence of fire or the exposure time. Simplified mechanical models were used to explain the behavior of the RC slabs during the tests.

## KEYWORDS

arching mechanism, fire exposure, RC circular slabs, residual conditions, static tests, tensile membrane action, ultrasonic pulse velocity

Discussion on this paper must be submitted within two months of the print publication. The discussion will then be published in print, along with the authors' closure, if any, approximately nine months after the print publication.

## 1 | INTRODUCTION

Fires in European tunnels, for example, in the Mont Blanc tunnel (France/Italy) in 1999 or in the Tauern tunnel (Austria) in 1999, have clearly shown the risks and

consequences of high thermal loads on reinforced concrete (RC) structures. The mechanical behavior of such structures subjected to a fire depends on many different factors, such as the constitutive behavior of concrete and steel and the type of structural member affected. Therefore, the investigation and understanding of RC structures exposed to fire has always been a challenge.<sup>1-8</sup>

Comprehensive experimental research at material level has been carried out in recent decades to test normal-strength concrete (NSC) subjected to elevated temperatures.<sup>9-20</sup> The use of high-strength concrete (HSC) has become increasingly popular compared to NSC due to its greater stiffness and strength (70–120 MPa). However, HSC is more sensitive to high temperatures due to its low porosity, which favors steam pressure build-up and increased susceptibility to explosive spalling. To avoid this, one commonly adopted solution is to add polypropylene (PP) microfibres.<sup>21,22</sup>

When concrete is exposed to elevated temperatures, its mechanical properties (such as strength and stiffness) are usually adversely affected.<sup>23</sup> However, the increased material deformability, another consequence of exposure to high temperatures, may help redistribute the stress at a structural level. Therefore, the considerable decrease in the mechanical properties of concrete may not directly result in a drastic decrease in the ultimate load-carrying capacity of the structural member.<sup>6,24</sup> Characterization of the material at elevated temperatures is therefore insufficient.

The literature contains many studies that have investigated the effect of fire on RC structural members, such as beams,<sup>25-30</sup> slabs,<sup>31-34</sup> or tunnel linings.<sup>35-38</sup> Despite all the research available, new recommendations and approaches for the design and assessment of concrete structures and structural components to protect against fire are still being published to this day.<sup>8,39-42</sup> Clearly the subject is a complex one, not yet fully investigated.

The investigation of RC slabs subjected to elevated temperatures is also of great interest for the Norwegian Public Roads Administration's *Ferry-free coastal route E39* project. This project is aimed at establishing a coastal highway route without ferry connections. New large concrete structures, including a submerged floating tunnel (SFT),<sup>43</sup> need to be built to cross the wide and deep fjords along the coast. It is then of interest to evaluate the combined action of fire and blast loads inside tunnels.<sup>44</sup> Due to the complexity of such extreme load conditions, this represents a great challenge.

In this context, RC slabs can be a representative component of the SFT concrete structure. A first and fundamental step is to achieve a full understanding of slab behavior at elevated temperatures under static loading conditions. The following experimental program consisting of three phases was therefore defined to investigate:

(i) the mechanical characterization of concrete at high temperatures,<sup>23</sup> (ii) the impact of the combination of fire and static loading on RC circular slabs (present study), and (iii) the impact of the combination of fire and dynamic loading on RC circular slabs.<sup>45</sup> The findings will make it possible to do the risk analysis and the feasibility study for the SFT in the E39 project.

Fire curves are used in the design of RC structures; for example, the hydrocarbon fire curve is typically used for the design of tunnels.<sup>46</sup> In the event of a hydrocarbon fire, stresses due to large thermal gradients during heating induce thermal damage to the structural member. Such damage is irreversible in concrete material, and may even increase during the cooling phase due to the appearance of additional thermal stresses.<sup>47,48</sup> In an accidental fire scenario inside a tunnel, the most thermally damaged part corresponds to the compressive side of the structural member's cross-section.<sup>41</sup> Testing in residual conditions, that is, with a cooling phase after heating, the steel reinforcement recovers all its mechanical properties after cooling while the concrete undergoes irreversible degradation. Testing with both the fire and the static load on the same side of the specimen, is therefore generally more conservative, since it represents a worst-case scenario for the overall structural behavior.

The main objective of this research was to investigate the influence of high temperatures on the load-bearing capacity of RC slabs. For this purpose, the structural response of RC circular slabs subjected to a static load in residual conditions, after exposure to a hydrocarbon fire, was investigated. Although the situation examined experimentally may be different to those observed in practice (Load Induced Thermal Strain [LITS] were not taken into account in this study), the experimental data presented in this work aims to define a reliable benchmark for numerical models which, upon numerical upscaling, will be instrumental for the design of tunnels under exceptional load conditions. Simplified mechanical models were used to understand the behavior of the specimen during the tests. The yield-line approach was used to evaluate the effect of high temperatures on the bending capacity of the slab. The contribution of the arching mechanism and tensile membrane action (TMA) on the structural response of the slab was also investigated.

## 2 | METHODOLOGY

### 2.1 | Experimental program

This study investigated the structural response of RC circular slabs after exposure to hydrocarbon fire. A total of 6 specimens were tested under static loading. Four of

**TABLE 1** Summary of the experimental campaign

Specimen ID	UPV test	Fire exposure (min)			Thermocouples (number)	Static test
		0	60	120		
S0-1	–	Y	–	–	–	Y
S0-2	–	Y	–	–	–	Y
S60-1	Y	–	Y	–	Y (4)	Y
S60-2	Y	–	Y	–	–	Y
S120-1	Y	–	–	Y	Y (4)	Y
S120-2	Y	–	–	Y	–	Y

Abbreviation: UPV, ultrasonic pulse velocity.

**TABLE 2** Concrete mix design

Material	Content (kg/m <sup>3</sup> )
CEM II/B-M 42.5R	223.40
CEM II/A-V 42.5N	193.33
Silica fume	12.89
Water	174.13
Aggregate 0–8	1026.48
Aggregate 8–16	754.95
Acrylic superplasticizer	3.06
Set retarding admixture	0.64
Polypropylene microfibers	1.00

them were subjected to fire exposure prior to the static test. Two reference non-exposed specimens were used for comparison. Two fire exposure times were considered ( $t = 60$  and  $120$  min). Thermocouples embedded in two specimens were used to measure the temperature distribution across the thickness. Ultrasonic pulse velocity (UPV) measurements were obtained in the specimens before and after exposure to the fire. All the slabs were tested at room temperature under quasi-static load conditions and the load-deflection response was measured. Table 1 summarizes the whole experimental campaign. The nomenclature of the specimens is defined as  $ST-n$ , where  $T$  is the fire exposure time (0, 60, or 120), and  $n$  is the number of the nominally identical test (1 or 2).

## 2.2 | Materials

Grade C45/55 concrete was used, with a water-cement ratio (w/c) of 0.42, and a maximum aggregate size ( $d_{max}$ ) of 16 mm. Table 2 details the concrete mix design and proportions. The aggregates (siliceous rock) included granite, gneiss, sandstone and siltstone. PP microfibers were also added to the mix (1 kg/m<sup>3</sup>). The density ( $\rho$ ) at 28 days after casting was 2370 kg/m<sup>3</sup>. The compressive

strength of the concrete was 73 MPa, calculated as the mean strength of three cylinders ( $D = 100$  mm,  $H = 200$  mm) at 202 days after casting.

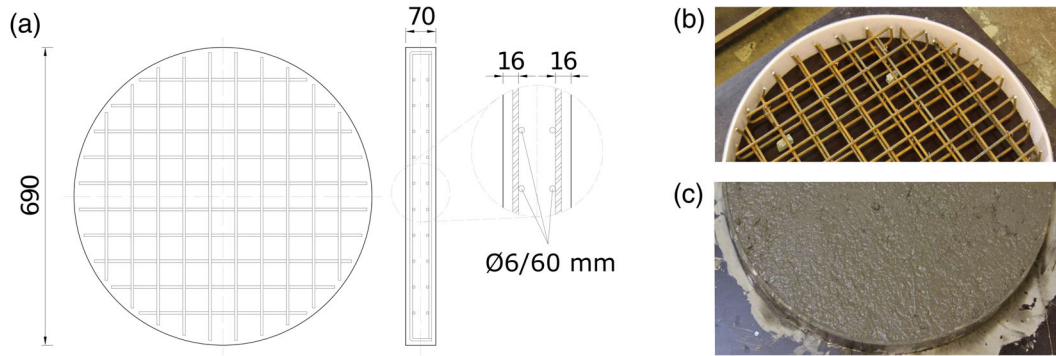
An extensive research on the mechanical properties of this type of concrete in residual conditions after single thermal cycles at elevated temperatures was previously performed by the same authors.<sup>23</sup> In that research, the evolution of the mechanical properties for four different temperatures (20°C, 200°C, 400°C, and 600°C) was evaluated. Standard concrete cylinders (100 × 200 mm) were subjected to uniaxial compressive testing (UCT) to measure the change in their modulus of elasticity, using the standard ISO procedure,<sup>49</sup> and their compressive strength. Uniaxial tensile testing (UTT) was also carried out on concrete cylinders (100 × 100 mm) to measure the evolution of direct tensile strength. Three nominally identical specimens were tested for each temperature level in the UCT, while two specimens were tested in the UTT. Further details on the test set-up and instrumentation can be found in Arano et al.<sup>23</sup>

The UCT and UTT were displacement-controlled, so complete stress-strain and crack opening displacement (COD) curves were obtained. This enabled the investigation of additional material properties, such as the specific compression and tension fracture energy at elevated temperatures and the evolution of internal damage. For the sake of brevity, these results are not given here, but they are extensively discussed in Arano et al.<sup>23</sup> In the same paper,<sup>23</sup> the relationship between the damage of concrete material and the UPV measurements is presented.

Traditional B450 steel was used for the reinforcement bars (Ø6). The mechanical properties of this type of steel were evaluated after single thermal cycles at elevated temperatures (200°C, 400°C, and 600°C). Eight steel reinforcing bars were tested in uniaxial tension in accordance with ISO standards,<sup>50</sup> using an INSTRON machine with a maximum capacity of 200 kN. Two nominally identical specimens were tested for each temperature level, where the yielding and ultimate strengths were measured. After the tests, the elongation at failure was measured in

**TABLE 3** Evolution of mechanical properties of concrete and steel after exposure at high temperatures

$T$ (°C)	$f_{c,T}$ (MPa)	$f_{ct,T}$ (MPa)	$E_{c,T}$ (MPa)	$f_{y,T}$ (MPa)	$f_{t,T}$ (MPa)	$\varepsilon_{su,T}$ (–)
20	73.0	3.6	27,609.4	500.9	648.8	0.32
200	64.7	4.5	25,777.1	585.2	699.9	0.25
400	37.3	2.4	15,139.7	565.2	660.7	0.31
600	21.3	1.2	7577.9	508.4	611.7	0.37

**FIGURE 1** (a) Geometry of the RC slab; (b) preparation of specimen, and (c) specimen after casting (units: mm). RC, reinforced concrete

accordance with ISO standards.<sup>50</sup> The tests were displacement-controlled using a high-accuracy transducer with a gauge length of 50 mm placed in the central part, which measured the elongation of the rebar until it reached 2%. An internal transducer in the machine was then used to follow the test until complete failure of the specimen.

Table 3 summarizes the average results of the main mechanical properties for both concrete and steel materials at different high temperatures. As seen, the compressive ( $f_{c,T}$ ) and tensile ( $f_{ct,T}$ ) strengths and the modulus of elasticity ( $E_{c,T}$ ) of this type of concrete all decrease considerably after exposure to high temperatures, unlike the results of the yielding ( $f_{y,T}$ ) and ultimate strength ( $f_{t,T}$ ) of the steel rebar, which confirms the strong recovery of the mechanical properties of this type of steel during the cooling phase.

### 2.3 | Geometry of the slabs

In the present study, the specimens tested were RC circular slabs of 690 mm diameter and 70 mm thickness. The slabs were reinforced with two orthotropic grids ( $\text{Ø}6/60$  mm in both  $x$  and  $y$  directions) top and bottom with a cover of 10 mm. Figure 1 shows the geometry and pictures of the specimen during preparation and after casting.

The specimen size and reinforcement layout were dictated by the dimensions of the equipment used for the

dynamic experimental testing part of the program, which is reported in Colombo et al.<sup>45</sup>

## 2.4 | Description of the tests

### 2.4.1 | Ultrasonic pulse velocity measurements

Direct UPV measurements were taken to quantify the stiffness reduction produced by the thermal exposure across the thickness of the specimen (Figure 2). UPV measuring devices (E49, CONTROLS Group, Italy), with two piezoelectric transducers (emitter and receiver) located on opposite surfaces of the slab, as shown in Figure 2b, were used. Gel was added between the transducer and the specimen's surface to ensure full acoustic contact. The measurements for each specimen were taken at six different locations (U1–U6) across the slab surface, before and after the fire tests. Points U1–U3 were located at 50 mm from the center of the specimen, and points U4–U6 were located at 170 mm from the center; see Figure 2a.

### 2.4.2 | Fire tests

Four specimens were exposed to fire prior to the static tests (Table 1). Hydrocarbon fire, typical of tunnels,<sup>46</sup> was applied by means of an electric gas burner to a centered

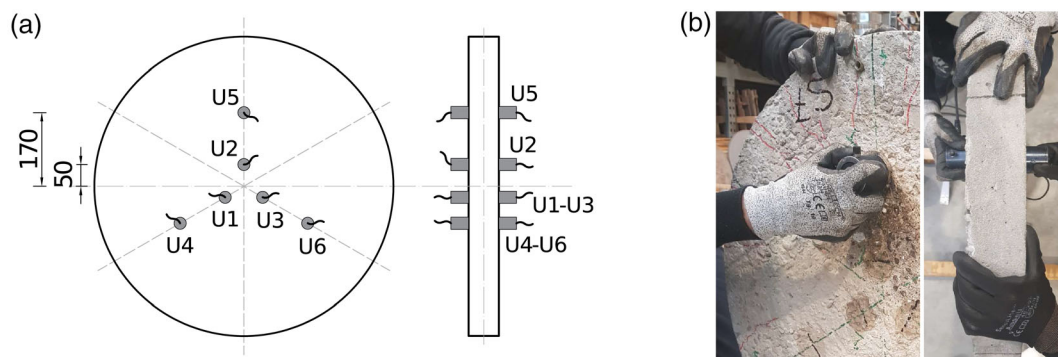


FIGURE 2 (a) Location of UPV measurements and (b) direct UPV acquisition (units: mm). UPV, ultrasonic pulse velocity

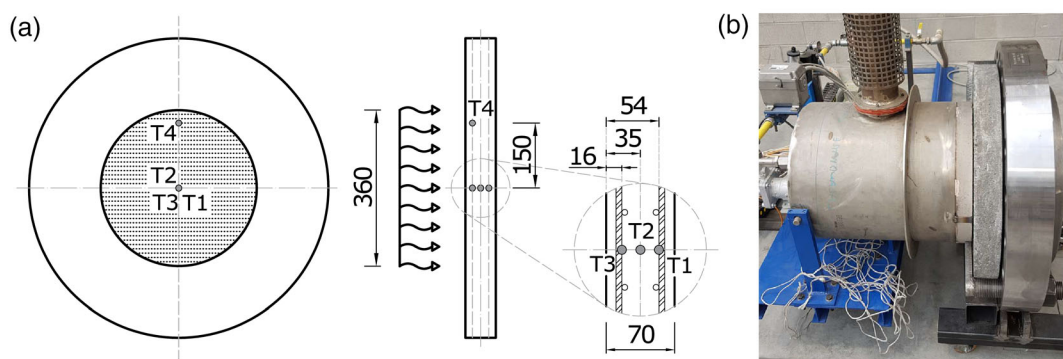


FIGURE 3 (a) Fire test set-up, with close-up of thermocouple positions and (b) burner equipment (units: mm)

circular region (diameter 360 mm) of what had been the top surface of the specimen during casting. A thermal sensor inside the burner was used to automatically regulate the intensity of the flame to achieve the predefined curve. Two fire cases were considered, with fire durations of 60 and 120 min, respectively. A fire exposure time of 120 min corresponds to the case of a tunnel as the primary structure with tanker truck traffic.<sup>46</sup> The specimens were able to freely expand during the tests and were naturally cooled in an open environment after the duration of the fire. Figure 3 presents the set-up for the fire tests, and a picture of the burner equipment. The test set-up required the specimens to be arranged vertically.

One of the two specimens in each fire exposure case was fitted with four temperature sensors (T1–T4) to measure the temperature distribution across the thickness of the slab. *Type-K chromel-alumel thermocouples* (0.91 mm thick) were embedded at three different depths during preparation of the specimens. Thermocouples T1–T3 were located at the center of the specimen, at a distance of 54, 35, and 16 mm from the “hot surface,” while T4 was located at 150 mm from the center at 16 mm from the “hot surface,” see Figure 3a. Temperature measurements were acquired with a time step of 1.146 s, obtaining an almost continuous temperature evolution throughout the tests.

### 2.4.3 | Static tests

Static tests were performed to evaluate the structural behavior of the six RC slabs. Two nominally identical tests were performed for each fire duration (60 and 120 min), in addition to two tests on the non-exposed specimens (Table 1). The tests were displacement-controlled by means of an electromechanical jack with a maximum capacity of 400 kN. The displacement rate was 50  $\mu\text{m/s}$  up to a load of 100 kN and 80  $\mu\text{m/s}$  up to failure. The vertical deflection of the specimens was measured by a linear variable differential transformer (LVDT) located at the center of the rear surface.

A circular steel ring of 320 mm in major diameter ( $d_e$ ) was used to apply the load. The specimens were loaded on the surface where the fire was previously applied (top surface during casting). A thin layer of neoprene was placed under the loading ring to distribute the load at the contact point between the steel ring and the specimen surface. The specimens were simply supported on a circular steel ring of 550 mm in minor diameter. Both rings had a radial thickness of 30 mm. Figure 4 shows the set-up for the static tests.

The dimensions of the support ring were chosen in accordance with the dimensions of the support scheme of the dynamic tests. This is why no neoprene layer was

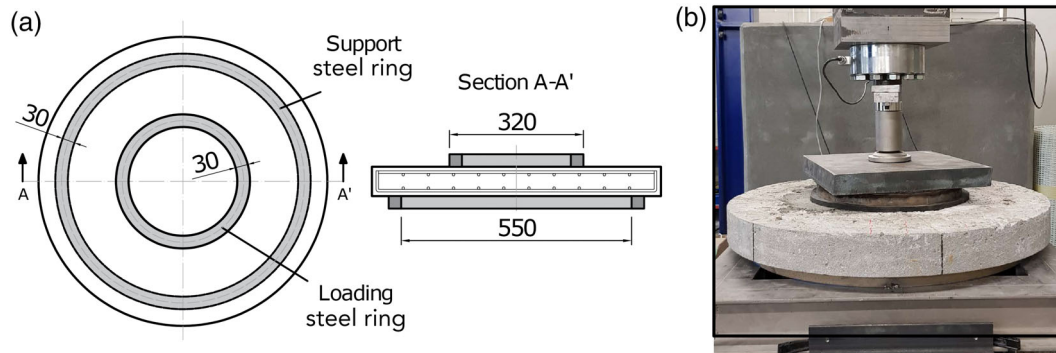


FIGURE 4 (a) Static test set-up and (b) picture during static test (units: mm)

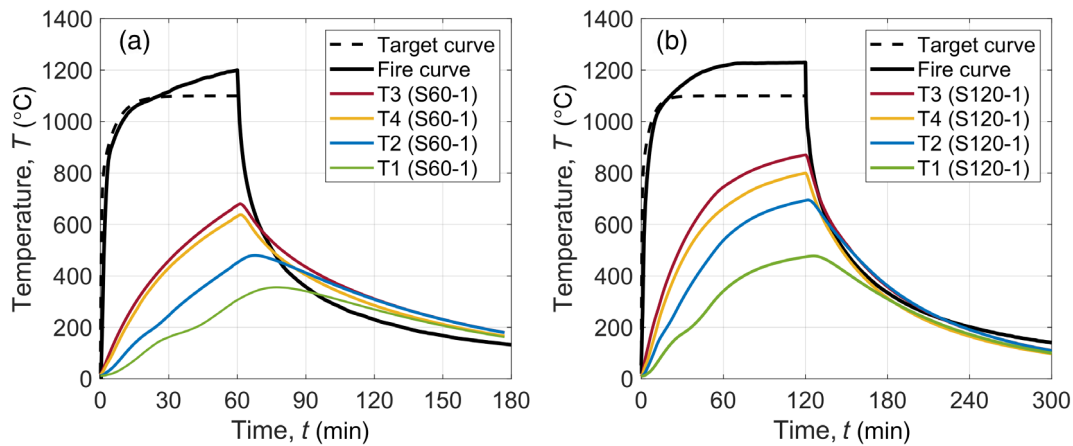


FIGURE 5 Temperature measurements from thermocouples T1–T4 in fire tests: (a) S60-1 and (b) S120-1

placed between the slab surface and the support ring. In the dynamic tests, the load is applied as a pressure wave, that is, a uniformly distributed load on the slab surface. Due to the difficulty of reproducing a uniformly distributed load under displacement control in a static test, the equivalent linear ring load was adopted to postpone the punching failure which would typically result from a concentrated load. A preliminary numerical investigation, which results are not shown here for the sake of brevity, was performed to determine the dimensions of the loading ring required to obtain a load-deflection behavior similar to the result of a distributed load, resulting in a loading ring with an external diameter  $d_e = 320$  mm.

### 3 | EXPERIMENTAL RESULTS

#### 3.1 | Fire tests results

Figure 5 presents the results of the temperature evolution measured during the fire tests on specimens S60-1 and S120-1. The different colors represent each of the four thermocouples (T1–T4) embedded in the specimens

(Figure 3). The figure also shows the fire curve (in black) for each test. In the 60-min fire test, temperatures of about  $680^{\circ}\text{C}$ ,  $640^{\circ}\text{C}$ ,  $480^{\circ}\text{C}$ , and  $360^{\circ}\text{C}$  were reached at locations T3, T4, T2, and T1, respectively (Figure 5a). In the 120-min fire exposure, the maximum temperatures measured at the same locations were about  $870^{\circ}\text{C}$ ,  $800^{\circ}\text{C}$ ,  $690^{\circ}\text{C}$ , and  $480^{\circ}\text{C}$  (Figure 5b). The measured temperature evolution up to 60 min was very similar in the two fire exposures, which indicates good repeatability in the tests.

The values from T1 to T3 were interpolated to obtain the temperature distribution across the whole thickness of the slab at different instants of time ( $t_i$ ). Equation (1) shows the exponential fit used, which describes the corresponding temperature value  $T$  for each point at a distance  $h$  from the “cold surface,” across the thickness of the slab. The coefficients  $a_i$  and  $b_i$  were calibrated from the experimental data and are shown in Table 4.

$$T = e^{\left(\frac{h-b_i}{a_i t}\right)} \quad (1)$$

Figure 6 shows the evolution of the temperature profile throughout the heating phase of the 60- and 120-min fire



**TABLE 4** Coefficients of the exponential fit of the temperature distribution across the thickness of the slab

$t_i$ (min)	Fire test: 60 min		Fire test: 120 min	
	$a_i$	$b_i$	$a_i$	$b_i$
30	35.95	-165.41	34.71	-163.59
60	48.12	-259.37	48.22	-266.20
90	-	-	58.34	-339.80
120	-	-	61.31	-363.01

tests at the central cross-section (T1–T3). Each color denotes a different instant during the test ( $t_i = 30, 60, 90,$  and  $120$  min). The experimental measurements are shown as filled circles, while the continuous line corresponds to the fitted values. The temperature values obtained at T4 are also shown for comparison, displayed as empty circles. The maximum experienced concrete temperature at the bottom and top surfaces as well as the steel temperatures (see sensors T1 and T3) can be read from Figure 6.

As expected, a hydrocarbon fire curve leads to a non-linear temperature profile across the cross-section due to the rapid increase in temperature. The results from the two cases investigated show that the profile remains non-linear throughout the whole test, though with a slight tendency toward a linear shape if  $t_i = 30$  and  $t_i = 120$  min in Figure 6b are compared. A big thermal gradient is observed between the two surfaces of the specimen, reaching a temperature difference of about  $720^\circ\text{C}$  for the 60-min fire exposure and about  $790^\circ\text{C}$  for the 120-min exposure time.

The large thermal gradient across the thickness and in the radial direction leads to non-homogeneous thermal expansion which induces additional stresses. Figure 7 shows the visible crack pattern for the different specimens after the fire tests. A similar crack pattern can be seen for all the specimens tested. On the exposed surface, radial cracks start some distance from the center and extend toward the edge of the slab in all directions. The non-exposed side, however, presents tensile cracks localized in the center of the specimen surface. Despite the presence of PP microfibers, minor explosive spalling was observed during the first minutes of the tests. The spalling was localized in a region of the exposed surface as highlighted in Figure 7.

Direct UPV measurements were taken across the thickness of the specimens, before and after exposure, to quantify the stiffness reduction caused by the fire. Table 5 summarizes the average pulse velocity before ( $v_0$ ) and after the fire test ( $v_t$ ), for both exposure times ( $t = 60$  and  $120$  min), together with the standard deviation

(SD) of the six points evaluated (U1–U6). The ratio between the two velocities is also shown.

The average pulse velocity before the fire test was  $4.70$  km/s. After the fire exposure, the pulse velocity has considerably decreased, especially after the longer exposure. The average pulse velocity of the specimens subjected to a 60-min fire test decreased to  $2.61$  km/s, while it decreased to  $2.21$  km/s after an exposure of  $120$  min. These represent reductions of about  $45\%$  and  $53\%$ , with respect to their values before the fire exposure. These UPV decreases quantify the cross-section stiffness reduction due to the material degradation under fire exposure.

### 3.2 | Static tests results

Figure 8 shows the complete load-deflection response for all the slabs subjected to the static test. Each nominally identical test is denoted with a different line type (solid or dashed), while the different colors represent the three fire exposure cases ( $0, 60$  and  $120$  min).

The load-deflection curves show two peaks corresponding to two separate mechanisms. The peak of the stiffer mechanism (point D) corresponds to the arching mechanism, while the peak of the ultimate load (point F) is related to TMA. The different stages of such mechanisms are indicated in the load-deflection curve of specimen S0-2 in Figure 8. Prior to cracking, the behavior of the slab is elastic (from A to B), until the first cracks appear at point B. In the intervals B–C and C–D, the slab exhibits an elastic–plastic phase, in which the arching mechanism is fully developed. The visible change of slope at point C is caused by the yielding of reinforcement. The maximum arching effect is achieved at Point D. After the rupture of the arch, the load considerably decreases. The remaining capacity (point E) corresponds to the pure bending capacity of the slab. TMA develops in the last stage (from E to F), increasing the load until the steel rebars reach their ultimate strain.<sup>51</sup> The behavior described was very similar for all the tested specimens, indicating that the same mechanisms were also at work in the slabs subjected to fire exposure.

Figure 9a shows a close-up of the load-deflection results. Figure 9b shows the relative average value of the arch peak load ( $P_{u,t}$ ) and the deflection at the arch peak load ( $\delta_{1,t}$ ) for the different exposure cases, with respect to the average values for the non-exposed specimens ( $P_{u,0}$  and  $\delta_{1,0}$ ).

The values of  $P_{u,t}$  and  $\delta_{1,t}$  are lower after fire exposure for all the specimens. The average arch peak load was  $327$  kN for the non-exposed slabs. This load was down to  $210$  and  $179$  kN after exposure to the 60- and 120-min fire

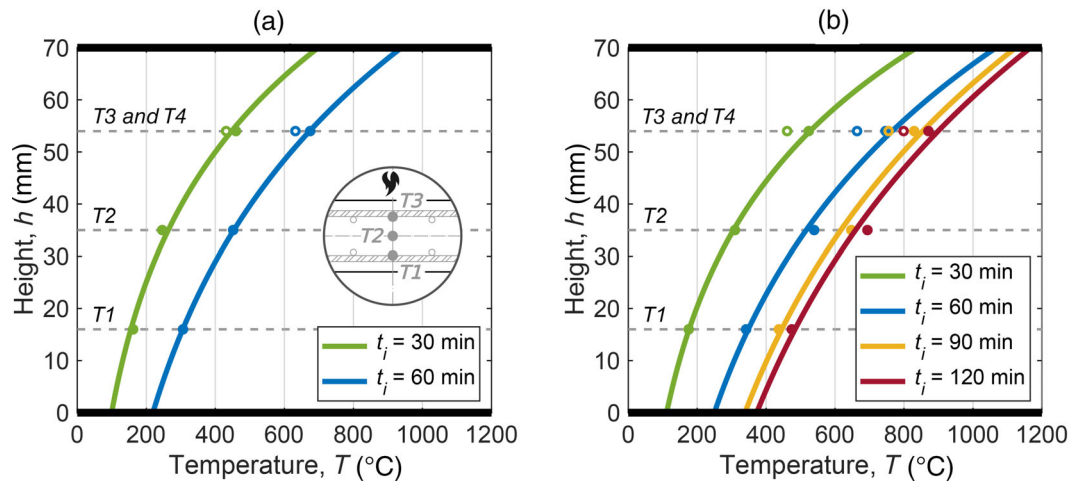


FIGURE 6 Temperature distribution evolution across the thickness for (a) 60-min and (b) 120-min fire test

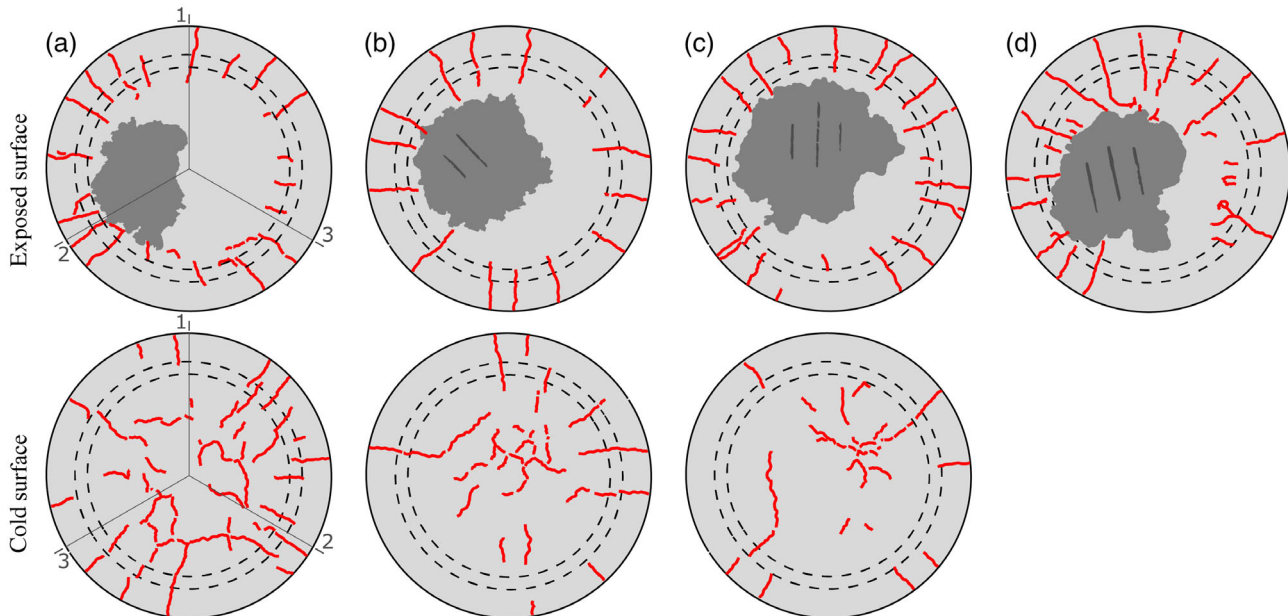


FIGURE 7 Crack pattern after fire tests: (a) S60-1, (b) S60-2, (c) S120-1, and (d) S120-2

TABLE 5 Average pulse velocity measurements (standard deviation in parentheses)

Specimen ID	Velocity before fire test, $v_0$ (km/s)	Velocity after fire test, $v_t$ (km/s)	Relative value $v_t/v_0$ (%)
S60-1	4.64 (0.04)	2.54 (0.33)	54.74
S60-2	4.73 (0.11)	2.68 (0.15)	56.66
S120-1	4.72 (0.33)	2.23 (0.38)	47.25
S120-2	4.71 (0.12)	2.20 (0.10)	46.71

tests, respectively. These values represent decreases of 36% and 45% in the peak load. The average deflection at such a load for the non-heated case is 14.4 mm. After fire exposure, the deflection was reduced to 7.9 and 7.7 mm, respectively representing decreases of 45% and 47%.

Despite the strong effect of fire exposure on the arching mechanism, Figure 8 shows a similar load-deflection trend when TMA develops, with the exception of specimen S0-1. The ultimate load was 286 kN for the other non-exposed slab (S0-2), which was similar to the average

**FIGURE 8** Complete load-deflection curve results for each static test

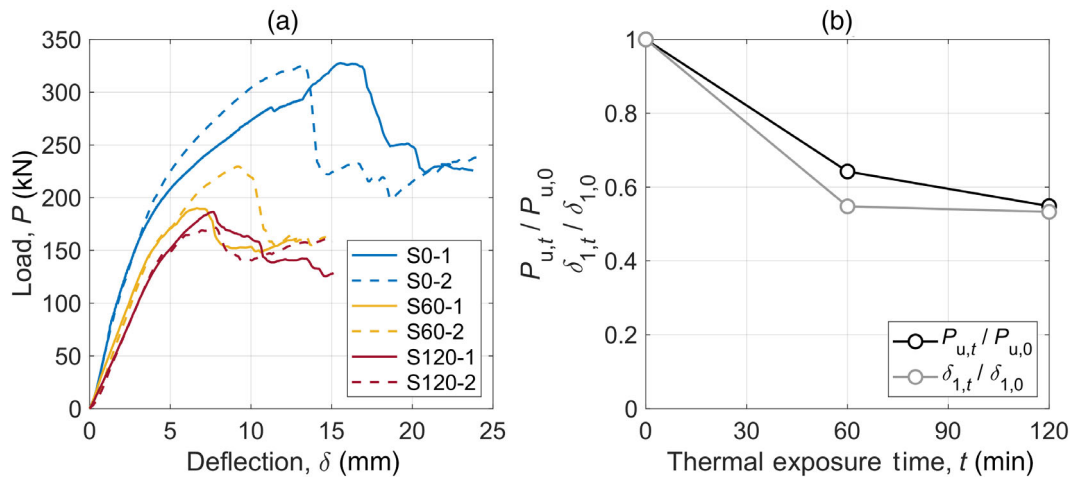
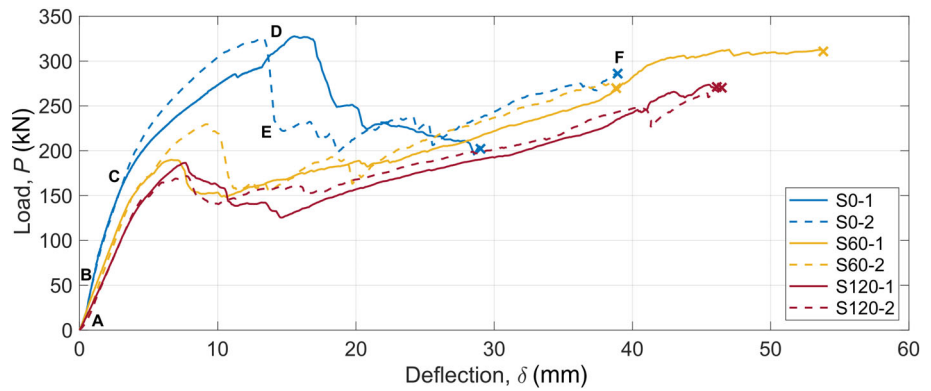


**FIGURE 9** (a) Close-up of load-deflection curves and (b) comparison of average failure load and deflection at failure load for each exposure time

ultimate load reached by the exposed specimens (294 and 272 kN, respectively), regardless of the fire exposure time. This is further evaluated in Section 5.2.

Figure 9a shows a change in the initial stiffness of the slab after fire exposure. While non-exposed specimens show an initial slope corresponding to elastic stiffness, the specimens that have been exposed to fire have reduced stiffness. When a specimen is subjected to fire, the material across the thickness is progressively exposed to high temperatures, and therefore the thermal damage increases across the thickness. The decrease in the initial stiffness can be quantified by analyzing the initial slope of the load-deflection curve. The results show an average decrease of about 35% after a fire exposure of 60 min, and about 50% after 120 min. These reductions are slightly lower than those obtained from the direct UPV measurements (Table 5) because they also consider the contribution of the steel reinforcement, which is characterized by negligible damage since the tests were performed in residual conditions. It is worth to note that the reduction on the

UPV measurements does not consider the strain profile of a bent cross-section but simply gives an average of the concrete degradation over the thickness.

Figure 10 shows pictures of all the specimens after the static tests. These pictures confirm that the same arch failure mechanism occurred for all the different tests, as highlighted in the comparison of the load-deflection responses.

## 4 | SIMPLIFIED APPROACH

### 4.1 | Description of analytical model

In order to comprehend and explain the results from the experimental tests, analytical calculations with simplified mechanical models were carried out. The yield-line method, first presented by Johansen,<sup>52</sup> was used, since it is a well-known approach commonly used for the moment analysis of RC slabs.<sup>53</sup> The yield-line pattern depends on the geometry and load conditions of the

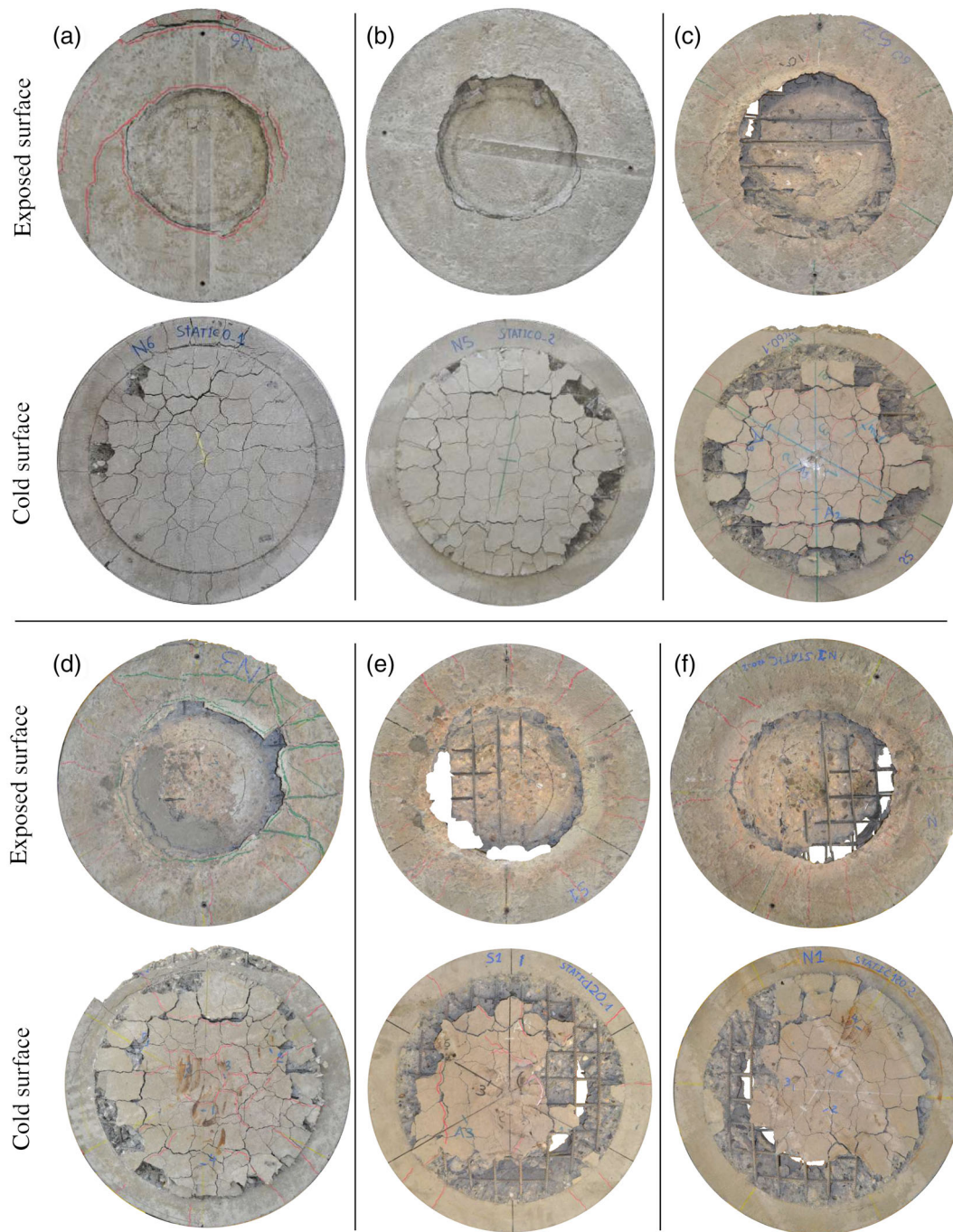


FIGURE 10 Failed specimens (a) S0-1, (b) S0-2, (c) S60-1, (d) S60-2, (e) S120-1, and (f) S120-2, after static tests

structure. In the case of the simply supported circular RC slabs evaluated in the present work, the yield pattern is shown in Figure 11.

The principle of virtual work is commonly used when applying the yield-line method to calculate the ultimate load. This method is based on the equilibrium between the work from the external loads and internal actions, when a virtual displacement  $\delta$  is assumed at a certain point in the slab. Following this procedure, the ultimate load  $P_f$  for the given slab is presented in Equation (2).

Since this method is widely used, the whole procedure is not described here for the sake of brevity.

$$P_f = \pi \left( 1 + \frac{R^*}{\bar{R}} \right) (m_x + m_y) \delta \quad (2)$$

In Equation (2),  $\bar{R}$  and  $R^*$  are the distances from the support to the load ring ( $\bar{R} = 115$  mm) and from the load to the center of the slab ( $R^* = 160$  mm), respectively. The moments  $m_x$  and  $m_y$  are the resistance moments of the

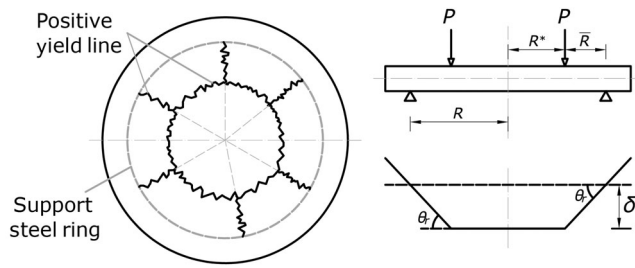


**FIGURE 11** Yield line pattern for circular RC slab concentrically loaded. RC, reinforced concrete

section in the two directions, which are the same in the case of an orthotropic reinforcement grid, characterized by the same reinforcement ratios  $\rho_x = \rho_y$ , neglecting the small difference between the reinforcement distance from the top surface  $d_x \cong d_y = 54 \text{ mm}$  ( $m_x = m_y = m$ ).

This method was applied for the three fire scenarios ( $t = 0, 60, \text{ and } 120 \text{ min}$ ). Assuming, as a simplification, no variation in the yield pattern, the moment resistance ( $m$ ) of the cross-section is the only changing variable between the scenarios. The moment resistance was calculated under the load ring, where the circular yield-line is located. The thermal damage was accounted for by including the temperature distribution measured experimentally in the calculation of the moment resistance. The moment obtained was assumed for the whole yield pattern.

The specimens were tested in residual conditions, with a cooling phase after the fire exposure. As previously described, steel material properties experience a great recovery for temperatures up to  $600^\circ\text{C}$ . Full recovery of the material performance was considered for both reinforcement layers, which is reasonable if evaluating the temperature results obtained, especially for the lower steel grid. Concrete properties, in contrast, differ considerably depending on the maximum temperature reached. The different thermal damage was then accounted for by dividing the compressive zone into several layers and defining the stress value for each layer depending on the temperature and strain level.

A stress-strain relationship based on uniaxial compressive tests was used for each temperature, following the procedure of the new draft of the Eurocode 2 Part 1-2.<sup>54</sup> In the code, the response of concrete to uniaxial compression at elevated temperatures is described using the relationship presented in Equation (3), where  $f_{c,\theta}$  and  $\varepsilon_{c1,\theta}$  are respectively the compressive strength and strain at maximum stress at a temperature  $\theta$ .

$$\varepsilon \leq \varepsilon_{c1,\theta} : \sigma(\theta) = \frac{3 \varepsilon f_{c,\theta}}{\varepsilon_{c1,\theta} \left( 2 + \left( \frac{\varepsilon}{\varepsilon_{c1,\theta}} \right)^3 \right)} \quad (3)$$

This relationship describes the concrete behavior up to  $\varepsilon_{c1,\theta}$ . The descending branch can be treated as linear until the ultimate limit concrete strain at the evaluated temperature,  $\varepsilon_{cu,\theta}$ . This material model was used, adopting the experimental values of  $f_{c,\theta}$ ,  $\varepsilon_{c1,\theta}$ , and  $\varepsilon_{cu,\theta}$  presented in Arano et al.<sup>23</sup> Figure 12a shows the good agreement between the adapted model and the experimental curves available for  $200^\circ\text{C}$ ,  $400^\circ\text{C}$ , and  $600^\circ\text{C}$ . For the other temperatures,  $\varepsilon_{c1,\theta}$  was exponentially fitted, as also reported by Felicetti et al.,<sup>11</sup> while  $\varepsilon_{cu,\theta}$  was linearly fitted. Figure 12b shows the resulting simplified 3D constitutive matrix.

A linear strain distribution in the sectional analysis of the cross-section was assumed, defining the maximum compressive strain in the concrete at the edge of the cross-section ( $\varepsilon_{c0}$ ) as  $\varepsilon_{c1,\theta}$ , and using the maximum temperature reached at that point. Eurocode 2 proposes a similar procedure,<sup>54</sup> alternatively estimating  $\varepsilon_{c0}$  as 40% higher than the strain at peak stress for the mean temperature reached across the section. The moment resistance of the cross-section for each fire case was then obtained, determining the bending capacity of the RC slab.

## 4.2 | Analytical results

This subsection presents a comparison between the bending capacity calculated for the different fire exposure cases using the yield-line method with the experimental results.

Figure 13 shows an example of the sectional analysis performed to compute the ultimate unitary bending moment of the cross-section, corresponding to the 60-min fire case. The temperature, strain and stress profiles are illustrated in Figure 13a-c. In the figure,  $T_{c,j}$ ,  $\varepsilon_{c,j}$ , and  $\sigma_{c,j}$  denote the temperature, strain, and stress value, respectively, for each layer ( $j$ ) of the concrete compressive zone, while the tensile contribution of concrete is neglected according to the traditional RC theory. The neutral axis (*N.A.*) is also shown. The strains and stresses in the two reinforcement layers are denoted  $\varepsilon_s$  and  $\sigma_s$  for the grid on the cold side, and  $\varepsilon'_s$  and  $\sigma'_s$  for the grid on the exposed side. Figure 13d is a close-up of the compressive zone to illustrate  $\sigma_{c,j}$ .

Following the analytical procedure described, the calculated moment resistance was 14.42, 10.23, and 9.19 kNm/m for the unexposed, 60-min fire, and 120-min fire cases, respectively. The yield-line solution presented in Equation (2) was then applied and the bending failure loads equal to 217, 154, and 138 kN for the three cases, respectively, were found.

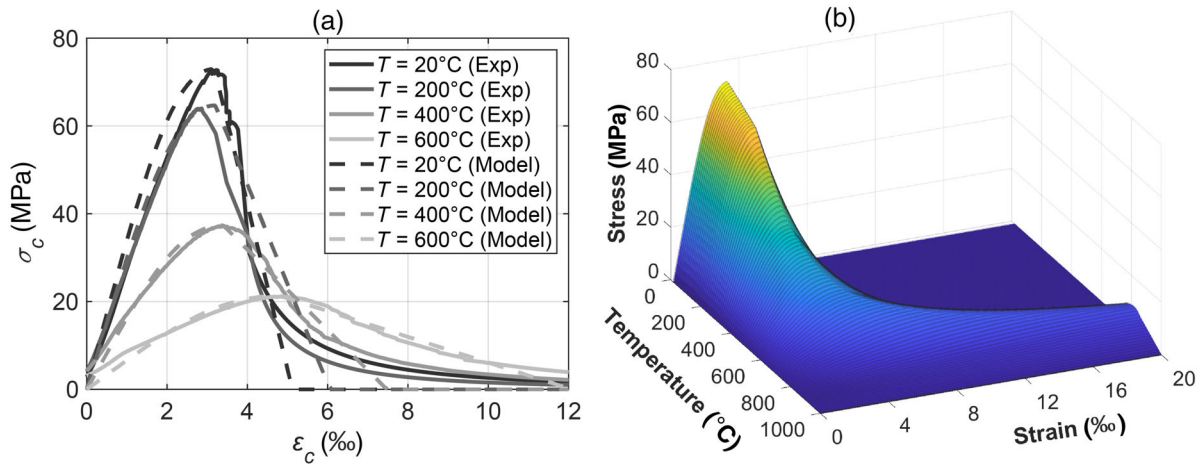


FIGURE 12 (a) Comparison between experimental curves<sup>23</sup> and the model adapted from Eurocode 2<sup>54</sup> and (b) generalized constitutive behavior for all temperatures

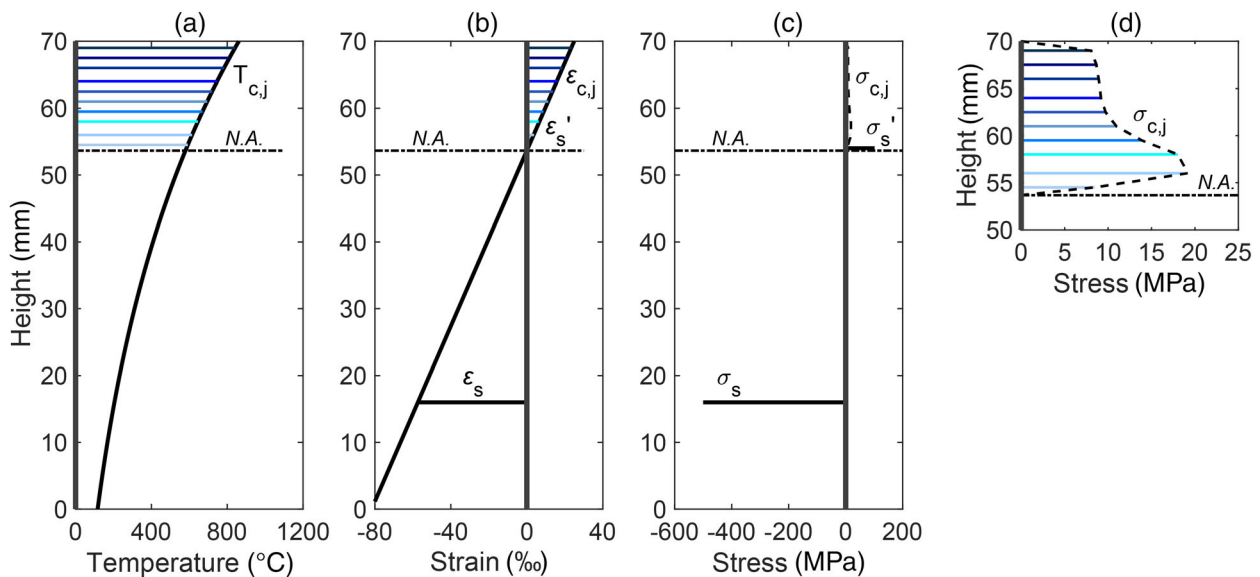


FIGURE 13 Sectional analysis for 60-min fire exposure: (a) temperature, (b) strain, and (c) stress profiles, and (d) close-up of the compressive zone

Figure 14 shows a comparison between the predicted values, represented as horizontal lines, and the experimental curves from the static tests. The values obtained using the analytical approach were very similar to the plateau stage of the experimental curves. As previously mentioned, the remaining capacity after the arching mechanism fails corresponds to the bending capacity of the slab, which is why there is good agreement between the analytical values and the experimental results.

## 5 | DISCUSSION OF RESULTS

The results obtained during the fire and static tests are discussed separately in this section. An evaluation of the crack

patterns obtained during the fire tests is firstly carried out. The influence of the high temperatures on the load-carrying capacity of RC slabs is then discussed by investigating the various stages of the load-deflection response.

### 5.1 | Cracking profile after the fire test

In this study, four RC slabs were exposed to a hydrocarbon fire applied in the central area of the specimen surface (Figure 3). The elevated temperatures induce an expansion of concrete and steel materials, which causes the formation of cracks across the specimens. The visible crack profile after the test can be divided into tensile and radial cracking.

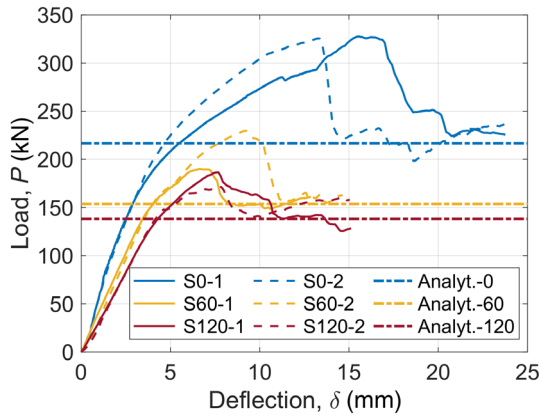


FIGURE 14 Comparison between analytical values and experimental results

Tensile cracks on the non-exposed surface commonly appear due to self-equilibrating stresses. A hydrocarbon fire, with its rapid increase of temperature, causes a non-linear temperature distribution across the thickness of the specimen. Virtually free thermal strain is thermal expansion at every point of the cross-section due to the temperature distribution. Since plane sections tend to remain plane, however, the actual deformation of the section is linear. The difference between the actual linear strain and the free nonlinear thermal strain is restrained, causing self-equilibrating stresses.<sup>55</sup> When the fire is acting on the specimen, the nonlinear distribution induces compressive stresses at both edges of the cross-section and tensile stresses in the middle. During the cooling phase, on the other hand, the two surfaces of the specimen undergo faster cooling, while the center of the section remains “hot,” inducing the opposite stresses. When the tensile stresses are higher than the concrete tensile strength, cracking occurs. As shown in Figure 7, these cracks are limited to the central area of the cold surface.

On the exposed hot surface, the tested specimens presented radial cracks. The origin of these cracks can be found if we examine the set-up used during the fire tests (Figure 3). The fire was applied in the central area ( $\text{Ø}360$  mm) of the total specimen surface ( $\text{Ø}690$  mm). The inner part is therefore subjected to a considerably higher temperature, and its greater thermal expansion induces, because of compatibility, a pressure on the outer part, causing tensile stresses. When these stresses reach the tensile strength of concrete, a crack occurs in the outer part of the surface and propagates toward the edge.

This phenomenon can be illustrated with the following simplified model to calculate the temperature difference necessary to form the first crack in the outer part. The model refers to the force method and adopts the

superposition principle to compute the internal stress of the specimen. As mentioned, the specimen is divided into two parts: an inner “hot” (H) area and an outer “cold” (C) area. Each part is assumed to have a uniform constant temperature and the difference in temperature between the two parts is defined as  $\Delta T$ . The radius of the inner part can be determined experimentally by analyzing the average radius ( $R_{avg}$ ) of the visible starting point of the various radial cracks in the tested specimens, as shown in Figure 15a. The radius is 225 mm. It can be seen that the crack initiation is very consistent between the different specimens.

Figure 15b shows a simplified sketch of the different contributions that have been considered in the application of the superposition principle. The inner core radius tends to enlarge ( $\Delta r_t$ ) due to thermal expansion and applies, because of compatibility, a pressure ( $p$ ) on the outer part that is colder and therefore characterized by less thermal expansion. This pressure causes a radial displacement in the outer ( $\delta_o$ ) and inner part ( $\delta_i$ ), which can be determined using the Lamé equations for thick-walled solids subjected to internal and external pressure, respectively.<sup>56</sup> Imposing the inner radius as  $r_i = R_{avg}$ , the displacements  $\delta_o$  and  $\delta_i$  for a unit pressure ( $p=1$ ) are obtained through Equations (4) and (5). The radius variation due to a thermal expansion is shown in Equation (6), where a negative sign is added since it acts in the direction opposite to  $\delta_i$ . In Equations (4) and (5),  $E_o$  and  $\nu_o$  are the modulus of elasticity and Poisson’s ratio of the outer part, while the modulus of elasticity and Poisson’s ratio of the inner part are denoted as  $E_i$  and  $\nu_i$ .

$$\delta_o = \frac{R_{avg}}{E_o} \left( \frac{r_o^2 + R_{avg}^2}{r_o^2 - R_{avg}^2} + \nu_o \right) \quad (4)$$

$$\delta_i = \frac{R_{avg}}{E_i} (1 - \nu_i) \quad (5)$$

$$\Delta r_t = -\alpha \Delta T R_{avg} \quad (6)$$

Since the two parts constitute the same solid specimen, the compatibility shown in Equation (7) must be fulfilled between the radius variation due to the pressure, and that due to the thermal expansion.

$$(\delta_o + \delta_i)p + \Delta r_t = 0 \quad (7)$$

The tensile stress at point  $R_{avg}$  can then be evaluated and imposed on the tensile strength of concrete ( $f_{ct}$ ). Doing this means that the gradient of temperature which produces the first crack ( $\Delta T_I$ ) can be obtained. If the same material properties are assumed for the whole specimen

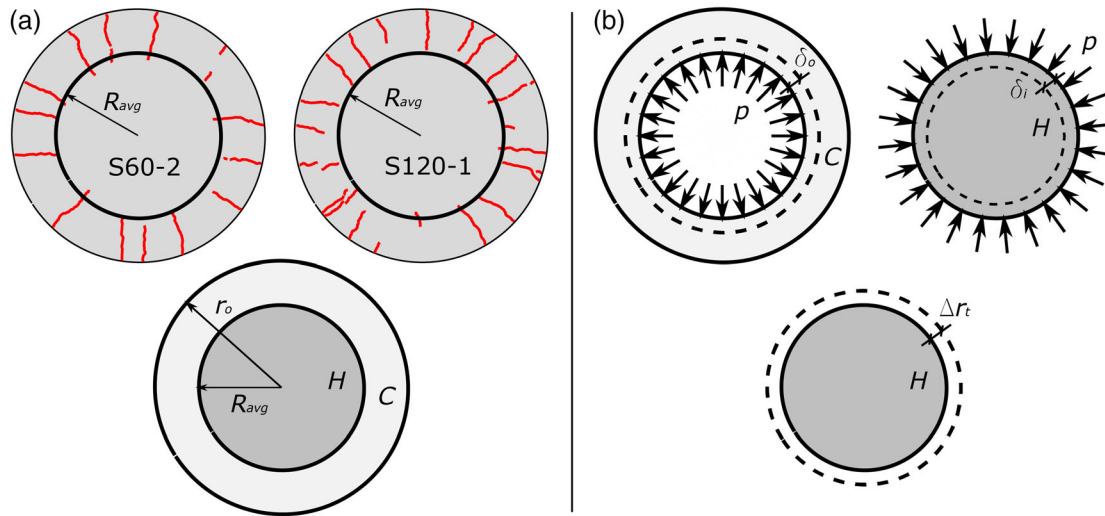


FIGURE 15 (a) Average crack initiation radius  $R_{avg}$  and (b) simplified model for evaluating the radial cracks

( $\nu_o = \nu_i = \nu$  and  $E_o = E_i = E$ ), which would be the case for lower temperatures (approximately below  $200^\circ\text{C}$ ), the value of the thermal gradient is obtained as in Equation (8).

$$\begin{aligned} \Delta T_I &= \frac{f_{ct}}{\alpha E} \left( 1 + \frac{r_o^2 - R_{avg}^2}{r_o^2 + R_{avg}^2} \right) \\ &= \frac{3.6}{1 \cdot 10^{-5} \cdot 27609} \left( 1 + \frac{345^2 - 225^2}{345^2 + 225^2} \right) = 18.3^\circ\text{C} \quad (8) \end{aligned}$$

As we have seen, the first crack occurs relatively early for a low-thermal gradient. As cracking occurs, the membrane stiffness of the outer part decreases, and so does the internal pressure between the two parts (Equation (7)). A new and reduced value for the pressure can be determined with the cracked stiffness. Since the stress generated with this new configuration is below the tensile strength of concrete, additional temperature gradient ( $\Delta T$ ) can be applied until the second crack occurs at another point at the same distance  $R_{avg}$  from the centre. By repeating this process and reaching the maximum temperature applied in the fire tests ( $1200^\circ\text{C}$ ), a multiple radial cracks formation configuration can be determined.

The mechanism described is not constant across the thickness since the nonlinear temperature distribution leads to different thermal gradients. However, this is a dominant action across the cross-section, and some of the radial cracks are also visible from the non-exposed side, see Figure 7.

This simplified model could be further developed to predict beforehand the dimension of the radial crack formation radius and the total number of cracks. Additional considerations would need to be taken into account, such as the decrease in the modulus of elasticity and tensile

strength of concrete at high temperatures in hot conditions, or variation in the Poisson's ratio. However, this is beyond the scope of this discussion, which was intended to explain the origin of the cracks related to high temperatures and the behavior of the specimen when subjected to a fire test with this test set-up.

## 5.2 | Structural behavior of reinforced concrete slabs

In this section, the influence of the fire on the load-bearing capacity and structural behavior of the RC slabs is discussed. Based on the load-deflection curves obtained, four main topics are here investigated. First, the effect of high temperatures on the yield point of the steel reinforcement and the bending capacity of the slabs is examined. The contribution of the arching mechanism and TMA to the response of the slab, and the effect that fire exposure has on them is then discussed.

### 5.2.1 | Yielding of reinforcement

A close-up of the complete set of experimental load-deflection curves obtained for all the specimens is presented in Figure 9a. The curves present a clear change of slope, which corresponds to the instant when the reinforcement starts to yield. Exposure to fire leads to a decrease in the yielding load, which was between 170 and 190 kN for the non-exposed slabs, but decreased to about 140 and 125 kN in the other slabs after exposure to a fire for a duration of 60 and 120 min, respectively.



Initially, one might attribute such a decrease in yielding load to possible thermal damage to the bottom steel grid caused by exposure to elevated temperatures. However, the experiments were undertaken in residual conditions, with a cooling phase prior to the static test. The centroid of the reinforcement on the non-exposed side was located at the same level as thermocouple T1. Figure 6 shows that the maximum temperature reached at that point was about 500°C. Results from tests on the mechanical properties of this type of steel in residual conditions showed a great recovery during the cooling phase,<sup>23</sup> in which the yielding strength after exposure to 600°C and cooling was comparable to that at 20°C. It is therefore reasonable to assume that the yielding strength in the tensile reinforcement grid was similar in all three cases investigated.

The decrease in the yielding load can be explained by considering the whole cross-section of the RC slab. The reduction in both stiffness and strength of concrete and the almost negligible damage experienced by steel reinforcement need a lower neutral axis to guarantee the translational equilibrium of the cross-section. This means that the internal lever arm, and therefore the bending moment, decrease with fire exposure despite the fact that the tensile strength of steel reinforcement is almost constant.

### 5.2.2 | Bending capacity

The bending capacity of the slab was calculated for the three cases using the sectional moment resistance. For the specimens subjected to fire exposure, reduced material properties were used. The evolution of material properties with temperature was taken from Arano et al.<sup>23</sup> where a detailed mechanical characterization of the same concrete material at high-temperature is reported. The measured temperature distribution was assumed equal throughout the yield pattern. This is obviously a simplification, since lower temperatures can be expected in regions far from the fire application. Another assumption is that the steel properties recovered their full performance after the cooling phase, which has been proved to be valid for temperatures up to 600°C. As shown in Figure 6, temperatures up to 800°C were measured at T4, which was also the centroid of the reinforcement on the exposed side. The properties of steel here could therefore be slightly lower than those assumed, in some parts of the slab. A more refined approach could be developed to get a complete overview of the temperature field across the slab. Numerical simulations of the fire tests could provide the temperature distribution across the thickness at every point of the specimen.

Despite the simplifications, good agreement was obtained in this study between the predicted values of bending capacity using the yield-line method and the experimental results from the static tests. The success of the analytical approach is mostly due to the behavior of the material at elevated temperatures being well understood. An extensive characterization, such as provided in Arano et al.<sup>23</sup> is needed both for simplified hand calculations and for advanced numerical simulations. In the literature, experimental studies investigating a specific type of material rarely cover a wide range of temperatures, which is why experimental tests, such as those presented in this study, are vitally needed to validate assumptions and simplified approaches in terms of material performance and overall structural behavior.

### 5.2.3 | Arching mechanism

The yield-line method is a widely studied approach, but in practice some RC slabs have a higher resistance than initially predicted. This may be due to the arching effect, where the formation of concrete struts between the load application and the supports results in an increase in the bending capacity of the structural member. In the present study, the appearance of the arching mechanism was due to the geometry of the specific test set-up used, and not caused by compressive membrane action.

The arching effect was observed in all the tested specimens. The average arch peak load reached by the RC slab was 327 kN for the non-exposed slabs, while it was 210 and 179 kN for the heat-damaged specimens. In comparison with the predicted bending capacity (217, 154, and 138 kN), the arching effect resulted in a load enhancement of 51% for the non-exposed specimens, but only 36% and 30% for the specimens exposed to 60 and 120 min, respectively.

The arching mechanism is typically obtained in RC beams with a low slenderness ratio ( $\lambda$ ) between the load application position and the support, and it also depends on the amount of reinforcement.<sup>57</sup> It can be expected to occur in an RC slab with this geometry, with a strut-and-tie system between the load application and the supports, as shown in Figure 16a. Equilibrium in the top node of the strut-and-tie system is achieved between the load applied and the compressive forces from the two concrete struts. The diagonal strut transfers the compressive force towards the support, which provides its vertical component. The tensile grid reinforcement acts as a tie equilibrating the horizontal forces in the bottom node. The mechanism fails when either the concrete strut on the top or the steel grid reaches the maximum capacity. Applying this mechanism to the whole RC slab, the struts

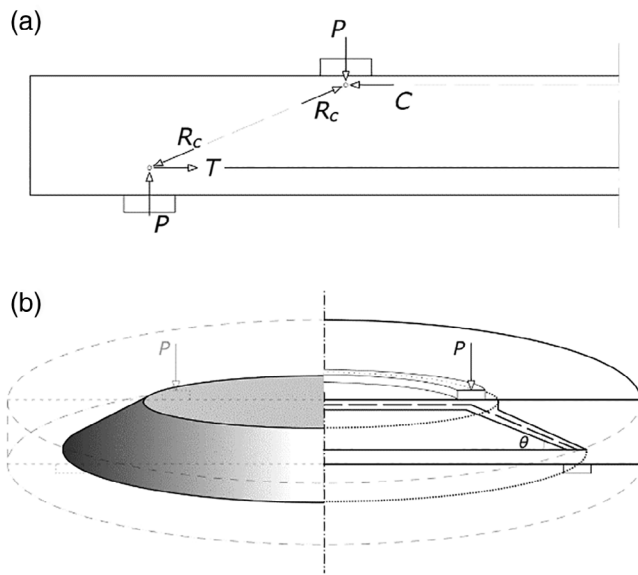


FIGURE 16 Sketch of the (a) sectional and (b) global arching mechanism

from the load application to the support are formed in all directions along the circumference, resulting in a truncated cone shape, see Figure 16b. The cone shape can be partially observed in Figure 10e,f.

As illustrated in Figure 9a, the load-deflection curve shows an almost linear first stage, until the yielding of the reinforcement, which is followed by a clearly nonlinear stage. This can be explained by taking into consideration the redundancy of the structure and, with it, the stress-redistribution. In this case, the circular geometry plays an important role. It is intuitive that the first point to yield is the central point of the reinforcement grid. Then, due to the circular geometry, all points located at the same distance from the central point will yield. Since the area of the yielding surface increases, a higher load can be applied. In this way, the yielding surface in the steel plate progressively increases together with the load that can be applied to the slab. The increased yield surface is transformed into a reduction in the stiffness of the plate, which leads to larger deflections. This explains the nonlinear change in stiffness once the yielding of the reinforcement grid starts.

The reinforcement used was an orthotropic grid, which could cause the stiffness reduction to behave slightly differently for each load increase. Theoretically, the reinforcement might even resist further load increase, until the total surface yielded. However, the experimental results indicate that what actually happened was that a failure of the concrete strut occurred when it reached a stress equal to the compressive strength of concrete.

Future research should include the frictional forces in the contact surface between the concrete and the steel

support ring since they may contribute to the arching effect. A numerical model could be developed by means of finite element software, including temperature-dependent material properties for the concrete and the steel. The fire exposure and static tests could be simulated and the results could be compared with the experimental findings. However, this falls outside the scope of the present study.

#### 5.2.4 | Tensile membrane action: ultimate load

Conventional structural design is focused on the evaluation of a global failure, such as bending failure or TMA. The former type of failure generally occurs at an early stage with small deflections, so TMA seems of little interest. In extreme loads like fire, however, the strength reserve of concrete structures plays an important role, allowing larger deflections. This is where tensile membrane or catenary action is of major interest, giving rise to a relevant research topic with respect to robustness analyses.<sup>58</sup>

Figure 8 shows the complete load-deflection response from the static tests. After the arch peak load is reached, the load rapidly decreases, which in this relatively thick slab can be attributed to the crushing of concrete.<sup>51</sup> As the deformations increase, the load-displacement curve enters a tensile membrane region where the load is almost entirely carried by tension in the reinforcement bars until the ultimate strain is reached.<sup>59</sup> In this vertically supported slab with no lateral restraint, the load at large deflections is carried by the TMA taking place at the center of the specimen, while a compressive supporting “ring” is formed around the perimeter of the slab by means of the compressive membrane action,<sup>60</sup> as schematically shown in Figure 17a. Load-deflection responses presented in Figure 8 have a similar trend to the typical relationship for restrained slabs presented in Guice and Rhomberg<sup>61</sup> (Figure 17b), where the distinct phases of behavior are highlighted and the flexural and arching contributions are identified.

The influence of elevated temperatures on the TMA mechanism after cooling does not follow the trend of the arching mechanism previously described. In contrast to the anticipated arch failure, both in load and deformation, the tensile membrane stage and ultimate load was only slightly affected by the fire exposure. As shown in Figure 8, similar values of ultimate load were reached in the various fire cases (286, 294, and 272 kN, respectively). This is a result of the almost negligible damage in the steel rebars after the fire exposure, combined with the fact that TMA mainly depends on the steel rebars

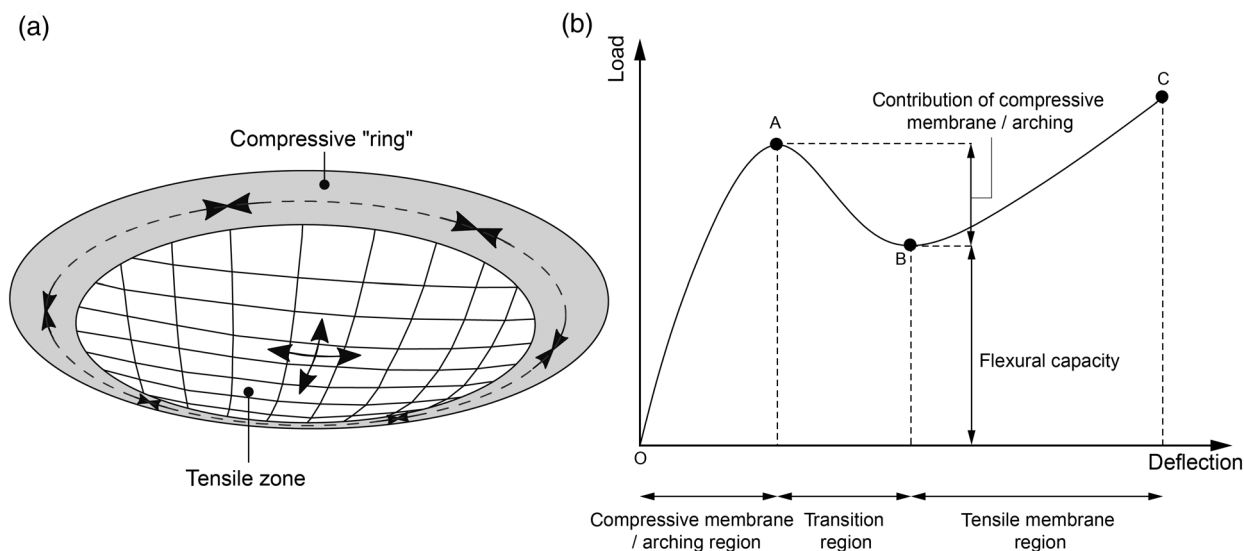


**FIGURE 17** (a) Sketch of the TMA mechanism and (b) typical load-deflection relationship for a restrained slab. TMA, tensile membrane action. *Source:* Adapted from Guice and Rhomberg<sup>61</sup>

behavior. This small influence is very relevant in terms of global resistance. While the fire exposure caused a decrease in the arch peak load (36% and 45% for the 60- and 120-min exposures, respectively), the ultimate load was 103% and 95% of the load obtained for the reference case (S0-2). This is a crucial aspect when considering safety and structural reliability.

In this study, the compressive “ring” was outside the fire region, so it was not strongly affected by the elevated temperatures. In an alternative scenario, the fire could act on the whole surface of the specimen, also damaging the concrete material in the perimeter. To study the possible effect on the TMA, we must evaluate the stress in the compressive “ring” for the tested slabs. Maximum stress is achieved when the ultimate load is reached. Assuming the compressive “ring” extends from the support to the edge, across the whole thickness, and using the steel yielding strength described in Section 2.2, a maximum stress of about 11 MPa is obtained in the concrete. As reported in Arano et al.,<sup>23</sup> this type of concrete withstands such stress for temperatures up to 800°C. So, considering the average temperature from the temperature distribution shown in Figure 6b, a similar ultimate load would probably be achieved in this RC slab due to TMA, even with a damaged compressive “ring.”

## 6 | CONCLUSIONS

This study investigated the influence of high temperatures on the load-bearing capacity of RC circular slabs in residual conditions. Fire tests were performed, applying a hydrocarbon fire with two different exposure times (60 and 120 min) to one side of the specimens. Static tests

were then performed on all the specimens, including the non-exposed reference slabs. The temperature distribution across the thickness and the load-deflection response were measured during the tests. Direct UPV measurements were made before and after the fire tests to quantify the cross-section stiffness reduction caused by the high temperatures. In addition, simplified mechanical models were used to discuss the effect of fire exposure on the structural response of the slab. Based on this research, the following conclusions were drawn:

- The maximum measured temperatures across the thickness ranged between 360°C and 680°C after the 60-min fire exposure, and between 480°C and 870°C after the 120-min fire exposure. A temperature difference between the two surfaces of the slab of some 720°C and 790°C was reached after 60- and 120-min fire tests, respectively. Nonlinear temperature distributions, characterized by large thermal gradients across the thickness, caused a similar tensile crack pattern on the non-exposed surface of all the fire-exposed specimens.
- After the fire tests, the specimens presented radial cracks on the exposed surface, which were caused by the temperature difference between the furnace area and the region of the specimen closer to the edge. Simplified calculations confirmed that a small thermal difference of about 15–20°C between the two regions was enough to explain the initiation and propagation of these radial cracks.
- An arching mechanism was obtained for all the specimens tested, resulting in a first peak in the load-deflection response. The arch peak load corresponded to a bending capacity enhancement of 51%, 36%, and 30%, respectively for the three exposure cases. The arching mechanism was negatively affected in the

presence of fire. The average arch peak load in the non-exposed slabs was 327 kN. After 60- and 120-min fire exposure, the peak load was reduced to 210 and 179 kN, respectively, which represents a decrease of 36% and 45%. The average results of deflection at the arch peak load were 14.4 mm for the non-heated case, and 7.9 and 7.7 mm after the 60- and 120-min fire exposure, representing reductions of 45% and 47%, respectively.

- Tensile membrane action enhanced the ultimate load of the slab. This mechanism was not greatly affected by the fire exposure, resulting in a similar average ultimate load for all three fire cases investigated (280, 294, and 272 kN, respectively), and confirming the robustness and structural reliability of this RC slab in residual conditions.
- Simplified calculations using the yield-line method showed good agreement with the experimental results after the loss of the arching mechanism. The use of temperature-dependent stress-strain curves of concrete for the sectional analysis proved to be a good approach for calculating the reduced bending capacity of the slab after exposure to fire.
- The experimental data presented in this paper are valuable in defining a reliable benchmark for the numerical models which, with numerical upscaling, will be instrumental for the design of the E39 submerged floating tunnel under exceptional load conditions.

## ACKNOWLEDGMENTS

The research presented in this paper was part of a PhD study funded by the Norwegian Public Roads Administration as part of the Coastal Highway Route E39 project.

## DATA AVAILABILITY STATEMENT

The data that support the findings of this study are available from the corresponding author upon reasonable request.

## ORCID

Matteo Colombo  <https://orcid.org/0000-0001-6457-7894>

Paolo Martinelli  <https://orcid.org/0000-0003-1029-7744>

Jan Arve Øverli  <https://orcid.org/0000-0002-3546-9058>

Max A. N. Hendriks  <https://orcid.org/0000-0001-9507-3736>

Marco di Prisco  <https://orcid.org/0000-0003-1779-2449>

## REFERENCES

1. Franssen JM. A study of the behaviour of composite steel-concrete structures in fire (in French). PhD thesis. Liège (Belgium): Liège University; 1987.
2. Harmathy TZ. Fire safety design and concrete. Harlow: Longman Scientific and Technical; 1993.
3. Terro MJ. Numerical modeling of the behavior of concrete structures in fire. *ACI Struct J*. 1998;95(2):183–93. <https://doi.org/10.14359/538>
4. Anderberg Y. Fire-engineering design of structures based on design guides. Proceedings of the 2nd international conference performance-based codes and fire-safety design methods, Maui, Hawaii; 1998.
5. Bamonte P, Felicetti R, Gambarova PG, Meda A. Structural behavior and failure modes of R/C at high temperature: R/C sections and 2-D members. In: Gambarova PG, Felicetti R, Meda A, Riva P, editors. Fire design of concrete structures: what now? What next?. Brescia: Starrylink; 2005. p. 159–74.
6. Felicetti R, Gambarova PG, Semiglia M. Residual capacity of HSC thermally damaged deep beams. *J Struct Eng*. 1999; 125(3):319–27. [https://doi.org/10.1061/\(ASCE\)0733-9445](https://doi.org/10.1061/(ASCE)0733-9445)
7. Khoury GA. Effect of fire on concrete and concrete structures. *Prog Struct Eng Mater*. 2000;2(4):429–47. <https://doi.org/10.1002/pse.51>
8. Bamonte P, Gambarova PG, Kalaba N, Tattoni S. Some considerations on shear and torsion in R/C structural members in fire. *J Struct Fire Eng*. 2018;9(2):94–107. <https://doi.org/10.1108/JSFE-01-2017-0019>
9. Abrams MS. Compressive strength of concrete at temperatures to 1600 F. SP25-02. In: Temperature and Concrete, ACI Spec Publ 25; 1971, p. 33–58.
10. Anderberg Y, Thelandersson S. Stress and deformation characteristics of concrete at high temperatures. 2. Experimental investigation and material behaviour model. Bulletin of division of structural mechanics and concrete construction, Bulletin 54. Lund: University of Lund; 1976. p. 1–84.
11. Felicetti R, Gambarova PG. The effects of high temperature on the residual compressive strength of high-strength siliceous concretes. *ACI Mater J*. 1998;95(4):395–406. <https://doi.org/10.14359/382>
12. Hager I, Pimienta P. Mechanical properties of HPC at high temperature. In: Gambarova PG, Felicetti R, Meda A, Riva P, editors. Fire design of concrete structures: what now? What next?. Brescia: Starrylink; 2005. p. 95–100.
13. Janotka I, Bágel L. Pore structures, permeabilities, and compressive strengths of concrete at temperatures up to 800°C. *ACI Mater J*. 2002;99(2):196–200. <https://doi.org/10.14359/11713>
14. Khaliq W, Kodur V. High temperature mechanical properties of high-strength fly ash concrete with and without fibers. *ACI Mater J*. 2012;109(6):665–74. <https://doi.org/10.14359/51684164>
15. Khoury GA. Compressive strength of concrete at high temperatures: a reassessment. *Mag Concr Res*. 1992;44(161):291–309. <https://doi.org/10.1680/mac.1992.44.161.291>
16. Khoury GA, Algar S. Mechanical behaviour of HPC and UHPC concretes at high temperatures in compression and tension. In: Proceedings of the ACI international conference on state-of-the-art in high performance concrete, Chicago; 1999.
17. Naus DJ, Graves HL. A review of the effects of elevated temperature on concrete materials and structures. In: Proceedings of 14th International Conference on Nuclear Engineering. 2008; 615–24. <https://doi.org/10.1115/ICONE14-89631>
18. Phan LT, Carino NJ. Mechanical properties of high-strength concrete at elevated temperatures. NIST internal report no. 6726. Gaithersburg, MD: Building and Fire Research Laboratory; 2001.
19. Sancak E, Sari YD, Simsek O. Effects of elevated temperature on compressive strength and weight loss of the light-weight concrete

- with silica fume and superplasticizer. *Cem Concr Compos.* 2008; 30(8):715–21. <https://doi.org/10.1016/j.cemconcomp.2008.01.004>
20. Schneider U, editor. RILEM-committee 44-PHT. Behaviour of concrete at high temperatures. Kassel: Department of Civil Engineering, Kassel University; 1985.
  21. Hager I, Mróz K. Role of polypropylene fibres in concrete spalling risk mitigation in fire and test methods of fibres effectiveness evaluation. *Materials.* 2019;12(23):3869. <https://doi.org/10.3390/ma12233869>
  22. Kalifa P, Chéné G, Gallé C. High-temperature behaviour of HPC with polypropylene fibres: from spalling to microstructure. *Cem Concr Res.* 2001;31(10):1487–99. [https://doi.org/10.1016/S0008-8846\(01\)00596-8](https://doi.org/10.1016/S0008-8846(01)00596-8)
  23. Arano A, Colombo M, Martinelli P, Øverli JA, Hendriks MAN, Kanstad T, et al. Material characterization approach for modeling high-strength concrete after cooling from elevated temperatures. *J Mater Civ Eng.* 2021;33(5):4021086. [https://doi.org/10.1061/\(ASCE\)MT.1943-5533.0003694](https://doi.org/10.1061/(ASCE)MT.1943-5533.0003694)
  24. Diederichs U, Jumppanen UM, Penttala V. Behavior of high strength concrete at high temperatures. Report no. 92. Helsinki: Helsinki University of Technology; 1989.
  25. El-Hawary MM, Ragab AM, El-Azim AA, Elibiari S. Effect of fire on flexural behaviour of RC beams. *Construct Build Mater.* 1996;10(2):147–50. [https://doi.org/10.1016/0950-0618\(95\)00041-0](https://doi.org/10.1016/0950-0618(95)00041-0)
  26. Eamon CD, Jensen E. Reliability analysis of RC beams exposed to fire. *J Struct Eng.* 2013;139(2):212–20. [https://doi.org/10.1061/\(asce\)st.1943-541x.0000614](https://doi.org/10.1061/(asce)st.1943-541x.0000614)
  27. Youssef MA, Diab MA, El-Fitiany SF. Shear capacity of RC beams at elevated temperatures. *Mag Concr Res.* 2015;67(22):1190–203. <https://doi.org/10.1680/mac.14.00163>
  28. Kodur VKR, Yu B, Solhmirzaei R. A simplified approach for predicting temperatures in insulated RC members exposed to standard fire. *Fire Saf J.* 2017;92:80–90. <https://doi.org/10.1016/j.firesaf.2017.05.018>
  29. Agrawal A, Kodur V. Residual response of fire-damaged high-strength concrete beams. *Fire Mater.* 2019;43(3):310–22. <https://doi.org/10.1002/fam.2702>
  30. Banerji S, Kodur V, Solhmirzaei R. Experimental behavior of ultra high performance fiber reinforced concrete beams under fire conditions. *Eng Struct.* 2020;208:110316. <https://doi.org/10.1016/j.engstruct.2020.110316>
  31. Bamonte P, Felicetti R, Gambarova PG. Punching shear in fire-damaged reinforced concrete slabs. SP265-16. Shear and torsion in concrete structures. Volume 265. Farmington Hills: ACI Special Publications; 2009. p. 345–66.
  32. Gambarova PG, Lo Monte F. Bending and shear behavior in one-way dapped-end reinforced concrete slabs. *ACI Struct J.* 2019;116(4):53–64. <https://doi.org/10.14359/51715572>
  33. Lo Monte F, Felicetti R, Rossino C. Fire spalling sensitivity of high-performance concrete in heated slabs under biaxial compressive loading. *Mater Struct.* 2019;52:1–11. <https://doi.org/10.1617/s11527-019-1318-0>
  34. Bamonte P, Fernández Ruiz M, Muttoni A. Punching shear strength of R/C slabs subjected to fire. In: Proceedings of the 7th international conference on structures in fire, Zurich; 2012, p. 689–98.
  35. Yan ZG, Zhu HH, Woody JJ, Ding WQ. Full-scale fire tests of RC metro shield TBM tunnel linings. *Construct Build Mater.* 2012;36:484–94. <https://doi.org/10.1016/j.conbuildmat.2012.06.006>
  36. Wang F, Wang M, Huo J. The effects of the passive fire protection layer on the behavior of concrete tunnel linings: a field fire testing study. *Tunn Undergr Sp Technol.* 2017;69:162–70. <https://doi.org/10.1016/j.tust.2017.06.021>
  37. Sakkas K, Vagiokas N, Tsiamouras K, Mandalozis D, Benardos A, Nomikos P. In-situ fire test to assess tunnel lining fire resistance. *Tunn Undergr Sp Technol.* 2019;85:368–74. <https://doi.org/10.1016/j.tust.2019.01.002>
  38. Felicetti R. Assessment methods of fire damages in concrete tunnel linings. *Fire Technol.* 2013;49:509–29. <https://doi.org/10.1007/s10694-011-0229-6>
  39. Kodur VKR. Innovative strategies for enhancing fire performance of high-strength concrete structures. *Adv Struct Eng.* 2018;21(11):1723–32. <https://doi.org/10.1177/1369433218754335>
  40. Agrawal A, Kodur VKR. A novel experimental approach for evaluating residual capacity of fire damaged concrete members. *Fire Technol.* 2020;56:715–35. <https://doi.org/10.1007/s10694-019-00900-1>
  41. Stucchi R, Amberg F. A practical approach for tunnel fire verification. *Struct Eng Int.* 2020;30(4):515–29. <https://doi.org/10.1080/10168664.2020.1772697>
  42. Kodur VKR, Naser MZ. Structural fire engineering. New York McGraw-Hill; 2020.
  43. Minoretti A, Xiang X, Johansen IL, Eidem M. The future of the tunnel crossing: the submerged floating tube bridge. *Struct Eng Int.* 2020;30(4):493–7. <https://doi.org/10.1080/10168664.2020.1775165>
  44. Colombo M, Martinelli P, di Prisco M. A design approach for tunnels exposed to blast and fire. *Struct Concr.* 2015;16(2):262–72. <https://doi.org/10.1002/suco.201400052>
  45. Colombo M, Martinelli P, Arano A, Øverli JA, Hendriks MAN, Kanstad T, et al. Experimental investigation on the structural response of RC slabs subjected to combined fire and blast. *Structures.* 2021;31:1030. <https://doi.org/10.1016/j.istruc.2021.02.029>
  46. ITA-AITES. Guidelines for structural fire resistance for road tunnels; 2004.
  47. Felicetti R, Gambarova PG, Sora MPN, Khoury GA. Mechanical behaviour of HPC and UHPC in direct tension at high temperature and after cooling. In: Proceedings of the 5th RILEM symposium on fibre-reinforced concretes, BEFIB 2000, Lyon, France: 2000, p. 749–758.
  48. Felicetti R, Gambarova PG. On the residual tensile properties of high-performance siliceous concrete exposed to high temperature. In: Proceedings of the International Work. Mechanics Quasi-Brittle Materials and Structures, Prague, Czech Republic; 1999, p. 167–186.
  49. ISO 1920-10:2010. Testing of concrete—part 10: determination of static modulus of elasticity in compression; 2010.
  50. ISO 15630-1:2019. Steel for the reinforcement and prestressing of concrete—test methods—part 1: reinforcing bars, rods and wire; 2019.
  51. Botte W, Caspeepele R, Gouverneur D, Taerwe L. Influence of membrane action on robustness indicators and a global resistance factor design. In: Proceedings of the 7th international conference on bridge maintenance, safety, management and life extension, IABMAS, Shanghai, China; 2014, p. 2038–2046.
  52. Johansen KW. Yield-line theory. London: Cement and Concrete Association; 1962.
  53. Kennedy G, Goodchild CH. Practical yield line design. Camberley: Concrete Centre; 2004.
  54. prEN 1992-1-2:2019-10. Eurocode 2: design of concrete structures—part 1-2: general-structural fire design. CEN/TC 250/SC 2/WG 1; 2019.
  55. El-Tayeb EH, El-Metwally SE, Askar HS, Yousef AM. Thermal analysis of reinforced concrete beams and frames. *HBRC J.* 2017;13(1):8–24. <https://doi.org/10.1016/j.hbrj.2015.02.001>

56. Lamé G, Clapeyron BPE. Mémoire sur l'équilibre intérieur des corps solides homogènes. In: Lamé G, editor. *Leçons sur la théorie mathématique l'élasticité des corps solides*. Paris: Hachette Livre; 1852. p. 465–562. <https://doi.org/10.1515/crll.1831.7.145>
57. Toniolo G, di Prisco M. *Reinforced concrete design to Eurocode 2*. Switzerland: Springer; 2017.
58. Gouverneur D, Caspeele R, Taerwe L. Experimental investigation of the load-displacement behaviour under catenary action in a restrained reinforced concrete slab strip. *Eng Struct*. 2013; 49:1007–16. <https://doi.org/10.1016/j.engstruct.2012.12.045>
59. Guice LK, Slawson TR, Rhomburg EJ. Membrane analysis of flat plate slabs. *ACI Struct J*. 1989;86(1):83–92. <https://doi.org/10.14359/2672>
60. Bailey CG. Membrane action of slab/beam composite floor systems in fire. *Eng Struct*. 2004;26(12):1691–703. <https://doi.org/10.1016/j.engstruct.2004.06.006>
61. Guice LK, Rhomberg EJ. An analogous model for slabs using a truss element. *Comput Struct*. 1989;31:767–74. [https://doi.org/10.1016/0045-7949\(89\)90211-3](https://doi.org/10.1016/0045-7949(89)90211-3)

## AUTHOR BIOGRAPHIES



**Assis Arano Barenys**, Norwegian University of Science and Technology, Department of Structural Engineering, Trondheim, Norway. Email: [assis.arano.barenys@norconsult.com](mailto:assis.arano.barenys@norconsult.com).



**Matteo Colombo**, Politecnico di Milano, Department of Civil and Environmental Engineering, Milan, Italy. Email: [matteo.colombo@polimi.it](mailto:matteo.colombo@polimi.it).



**Paolo Martinelli**, Politecnico di Milano, Department of Civil and Environmental Engineering, Milan, Italy. Email: [paolo.martinelli@polimi.it](mailto:paolo.martinelli@polimi.it).



**Jan Arve Øverli**, Norwegian University of Science and Technology, Department of Structural Engineering, Trondheim, Norway. Email: [jan.overli@ntnu.no](mailto:jan.overli@ntnu.no).



**Max A.N. Hendriks**, Norwegian University of Science and Technology, Department of Structural Engineering, Trondheim, Norway. Email: [max.hendriks@ntnu.no](mailto:max.hendriks@ntnu.no).



**Terje Kanstad**, Norwegian University of Science and Technology, Department of Structural Engineering, Trondheim, Norway. Email: [terje.kanstad@ntnu.no](mailto:terje.kanstad@ntnu.no).



**Marco di Prisco**, Politecnico di Milano, Department of Civil and Environmental Engineering, Milan, Italy. Email: [marco.diprisco@polimi.it](mailto:marco.diprisco@polimi.it).

**How to cite this article:** Arano Barenys A, Colombo M, Martinelli P, Øverli JA, Hendriks MAN, Kanstad T, et al. Failure characteristics of reinforced concrete circular slabs subsequently subjected to fire exposure and static load: An experimental study. *Structural Concrete*. 2022. <https://doi.org/10.1002/suco.202200054>